Article

Comparison of the Surface Properties of Hydrothermally Synthesised Fe$_3$O$_4$@C Nanocomposites at Variable Reaction Times

Sadiq Sani [1,2], Rohana Adnan [1,*], Wen-Da Oh [1] and Anwar Iqbal [1]

1 School of Chemical Sciences, Universiti Sains Malaysia (USM), Penang 11800, Malaysia; sadiqsani123@gmail.com (S.S.); ohwenda@usm.my (W.-D.O.); anwariqbal@usm.my (A.I.)

2 Department of Applied Chemistry, Federal University Dutsin-Ma, Dutsinma P.M.B. 5001, Nigeria

* Correspondence: r_adnan@usm.my

Abstract: The influence of variable reaction time (t_r) on surface/textural properties (surface area, total pore volume, and pore diameter) of carbon-encapsulated magnetite (Fe$_3$O$_4$@C) nanocomposites fabricated by a hydrothermal process at 190 °C for 3, 4, and 5 h was studied. The properties were calculated using the Brunauer–Emmett–Teller (BET) isotherms data. The nanocomposites were characterised using Fourier transform infrared spectroscopy, X-ray diffraction analysis, thermogravimetry, and scanning and transmission electron microscopies. Analysis of variance shows t_r has the largest effect on pore volume (F value = 1117.6, p value < 0.0001), followed by the surface area (F value = 54.8, p value < 0.0001) and pore diameter (F value = 10.4, p value < 0.001) with R^2-adjusted values of 99.5%, 88.5% and 63.1%, respectively. Tukey and Fisher tests confirmed t_r rise to have caused increased variations in mean particle sizes (11–91 nm), crystallite sizes (5–21 nm), pore diameters (9–16 nm), pore volume (0.017–0.089 cm^3 g^{-1}) and surface area (7.6–22.4 m^2 g^{-1}) of the nanocomposites with individual and simultaneous confidence limits of 97.9 and 84.4 (p-adj < 0.05). The nanocomposites' retained Fe–O vibrations at octahedral (436 cm^{-1}) and tetrahedral (570 cm^{-1}) cubic ferrite sites, modest thermal stability (37–60 % weight loss), and large volume-specific surface area with potential for catalytic application in advanced oxidation processes.

Keywords: ANOVA model; heating temperature; hydrothermal synthesis; magnetic nanocomposite; reaction time; surface properties

1. Introduction

In recent years, concerted efforts have been made to develop magnetite (Fe$_3$O$_4$) nanocomposite materials with improved surface properties suitable for specific applications in diverse fields. As nontoxic, biocompatible, and superparamagnetic materials of relatively high chemical stability, Fe$_3$O$_4$ nanocomposites find applications in biotherapy and biomedicine [1,2], drug targeting and delivery [3,4], catalysis [5–7], energy storage and release [8,9], environmental remediation [10], ultrafiltration membrane separation [11] and microwave absorption [12,13].

Fabrication of carbon-encapsulated magnetite nanocomposite materials (Fe$_3$O$_4$@C) by hydrothermal treatment is a popular method of rendering prevention to the parent Fe$_3$O$_4$ NPs from agglomeration and deterioration in chemical stability, thereby maintaining their effective surface properties, making them compatible for applications in both inorganic and organic processes. It involves synthesising Fe$_3$O$_4$@C nanostructures by heating at reaction temperatures and pressures above the ambient conditions of boiling water for a given reaction time, with the mixture of precursors in aqueous media as reported in the literature [14,15]. The method depends on precursor concentrations, the nature of the aqueous solvent, the stabilising agent, the type of precursor, the heating temperature, and the reaction time, which considerably influence the final products. It gives relatively low

product yields compared to the co-precipitation that produces nanocomposites with a weak crystal structure [16,17]. However, unlike the "low temperature" co-precipitation technique, the temperature–pressure synergistic effect in the hydrothermal approach offers a one-step route for producing magnetic nanocomposites of high crystallinity and removing the need for post-annealing [18,19].

However, several works have reported hydrothermal treatments using one-off levels of the process parameters (reaction temperature, reaction time, etc.) without setting them at variable levels to optimise their influences and compare their efficiencies in the fabrication of Fe_3O_4@C nanocomposites with defined surface characteristics. For example, several heating temperature–reaction time pairs reported for hydrothermal synthesis of Fe_3O_4@C include 180 °C for 14 h [20], 170 °C for 4 h [21], 600 °C for 4 h [22], 210 °C for 48 h [23], 160 °C for 10 h [24] and 180 °C for 24 h [25]. One-factor-at-a-time (OFAT) design optimisation of a hydrothermal process with few parameters furnishes optimal responses that are more reliable, minimises costs and maximises the utility of resources required to run the experiments. The lower the number of input parameters, the fewer are the runs and the resources for the experiments [26].

Therefore, fewer efforts were channelled into the use of OFAT design to optimise the effects of a limited number of independent factors (e.g., reaction time, temperature, amounts of Fe_3O_4 NPs precursor, amount of glucose precursor, etc.) on the surface characteristics of the carbon-encapsulated magnetite nanocomposites obtained via conventional hydrothermal synthesis. For instance, Subramanian et al. [27] accomplished the hydrothermal synthesis of MnO_2 by starting with well-mixed aqueous solutions of $MnSO_4 \cdot H_2O$ and $KMnO_4$ by loading into an oven preheated at 140 °C to evaluate the influence of variable reaction time (1–18 h) on the end material.

Thus, the main objectives of this work are to conduct the hydrothermal synthesis of Fe_3O_4@C composite samples and to statistically compare the dependence of their selected surface properties (surface area, total pore volumes and pore diameters) on variable reaction time at a fixed temperature using one-way analyses of variance (ANOVA). Based on the data gathered from the literature, three different reaction times were selected (3, 4, and 5 h). Tukey simultaneous tests and Fisher individual tests were also conducted to determine the differences in the means of the properties for comparison. The reaction time dependent mesoporosity, monodispersity, shape controllability, and stability of the as-synthesised Fe_3O_4@C nanocomposite samples were further ascertained by performing morphological and structural elucidations using suitable instrumental analyses.

2. Materials and Methods

2.1. Materials

Nitric acid (HNO_3), ethanol (C_2H_5OH, 95 %), anhydrous (D+)-glucose ($C_6H_{12}O_6$) and ethylenediamine ((H_2NCH_2)$_2$) were supplied by HmbG Chemicals, Kuala Lumpur, Malaysia. Ethylene glycol (($HOCH_2$)$_2$), sodium acetate (CH_3COONa) and ferric chloride hexahydrate ($FeCl_3 \cdot 6H_2O$) were purchased from Bendosen Laboratory Chemicals, Kuala Lumpur, Malaysia. The as-received analytical grade pure chemical reagents and deionised water were used in the entire experimental procedures.

2.2. Synthesis of Fe_3O_4@C Nanocomposite

Following the procedure mentioned elsewhere in the literature, mesoporous Fe_3O_4@C nanoparticles were prepared using a two-step process involving solvothermal and hydrothermal processes [28,29]. A solvothermal approach was first utilised to fabricate magnetite NPs. Weighed amounts of $FeCl_3 \cdot 6H_2O$ (1.0 g) and anhydrous CH_3COONa (4.0 g) were dissolved in a mixture of ethylene glycol (27 mL) and ethylenediamine (3 mL) under vigorous magnetic stirring at 1000 rpm for at least 30 min to form a homogenised clear yellow solution. The resulting solution was heated at 220 °C for 2 h in a 50mL tightly sealed, Teflon-lined stainless-steel autoclave before cooling to room temperature under a cold tap water jet. The as-synthesised black magnetite nanoparticles were separated from

the mixture using a magnet, washed copiously six times in a row with deionised water and ethanol, oven dried at 70 °C for 12 h under vacuum, and stored in an air-tight sample bottle placed in a desiccator for further processing.

The synthesis of the Fe_3O_4@C nanocomposites was carried out by first immersing 0.23 g (0.001 mol) of Fe_3O_4 NPs in 0.1 M HNO_3 solution for 5 min. Then, the nanoparticles were separated using a magnet and washed three times with deionised water. Then, the Fe_3O_4 NPs and 3.61 g (0.02 mol) of glucose were dissolved in 40 mL of deionised water under vigorous stirring for at least 10 min to homogenise the mixture. The mixture was oven-heated at 190 °C for the reaction time (t_r) of 3 h in a 50 mL Teflon-sealed autoclave in an oven. The as-obtained magnetic composite was then allowed to cool naturally, separated with a magnet, washed three times with deionised water and ethanol and oven-dried at 60 °C for 12 h under vacuum. The same procedure was repeated two more times under the same hydrothermal conditions for t_r values of 4 and 5 h. The three Fe_3O_4@C nanocomposites obtained were labelled as Fe_3O_4@C-$T_{190}t_3$, Fe_3O_4@C-$T_{190}t_4$ and Fe_3O_4@C-$T_{190}t_5$.

2.3. Instrumental Analyses

The characteristic chemical bonds in the Fe_3O_4@C-$T_{190}t_3$, Fe_3O_4@C-$T_{190}t_4$ and Fe_3O_4@C-$T_{190}t_5$ nanocomposites were elucidated in the range of 400–4000 cm^{-1} using a Fourier transform infrared (FTIR) spectrophotometer (Perkin Elmer System 2000 FTIR). The powdered samples of translucent pellets were prepared by mixing the sample with dry KBr followed by hydraulic compression and then inserted into the sample holder of the spectrophotometer for analyses.

The XRD tests of the as-synthesised nanocomposites samples were carried out on a fully automated X-Ray Diffractometer (Bruker's D8 Advance, Bruker Corporation, Billerica, MA, USA) located at the Makmal Pencirian Bahan Bumi, Centre for Global Archaeological Research, Universiti Sains Malaysia. Powdered samples were first prepared in the shape of a circular disc (25 mm diameter) by hydraulic compression, followed by insertion into the sample holder for examination. Mounted flat on a glass slide, the circular discs were gently squeezed parallel to the holder's surface. The XRD tests were conducted at a scanning velocity of 0.04 °C sec^{-1} for 25 min using the Cu-K_α radiation source (λ = 1.54060 Å), 40 kV voltage, 40mA current and 2θ scanning range of 10–70° at room temperature (25 °C).

Datasets on thermogravimetric analysis (TGA) and derivative thermogravimetry (DTG) were collected on a thermogravimetric analyser (Perkin Elmer STA 6000 model, PerkinElmer Inc., Waltham, MA, USA), domiciled at the School of Chemical Sciences, Universiti Sains Malaysia. The analyses were conducted by heating in air at 80 mL min^{-1}. The heating was carried out from 30 to 900 °C at a rate of 10 °C min^{-1}, followed by holding the temperature for 5.0 min at 900 °C.

A scanning electron microscope (Quanta FEG 650 SEM, FEI Company, Hillsboro, OR, USA) fitted with an energy-dispersive X-ray spectroscopy method (Oxford X-Max 50 mm^2 EDX, Oxford Instruments, Oxford, UK) was used to investigate the morphology and elemental analysis of the nanocomposites. The surface morphologies of the nanocomposites were further observed by employing an energy-filtered transmission electron microscope (Zeiss Libra 120, Carl Zeiss NTS GmbH, Oberkochen, Germany). The resulting energy-filtered transmission electron microscopy (EFTEM) micrographs were used to study the particle size distribution of the nanocomposites. The samples were sonicated in ethanol for 5 min to prepare ethanolic dispersions of the nanocomposites, subsequently spread on the copper grid surfaces and inserted into the electron transmission microscope.

The porosimeter (ASAP 2020 V4.01 H, Micromeritics Instrument Corporations, Norcross, GA, USA) available at the School of Chemical Sciences, Universiti Sains Malaysia, was employed to perform nitrogen adsorption–desorption analyses on the samples. The multilayer adsorption isotherm plots obtained by applying the Brunauer-Emmett-Teller (BET) equation to the resulting nitrogen physisorption data were used to determine the specific pore volume, pore size and surface area of the dried powdered nanocomposite

samples. The samples were degassed at 383 K for 6 h under vacuum before sample analysis and data collection.

3. Results and Discussion

3.1. Spectroscopic and Surface Characteristics of the Fe_3O_4@C Nanocomposites

The surface properties of the three as-synthesised nanocomposite samples Fe_3O_4@C-$T_{190}t_3$, Fe_3O_4@C-$T_{190}t_4$, and Fe_3O_4@C-$T_{190}t_5$ were evaluated following a one-factor-at-a-time (OFAT) design approach using various complementary instrumental methods of analysis.

3.1.1. Fourier Transform Infrared Spectroscopy

Figure 1 illustrates the FTIR spectra of the as-synthesised Fe_3O_4 NPs and Fe_3O_4@C nanocomposites. Assignments of the major absorption bands observed at 436 and 570 cm^{-1} in the spectrum of the parent magnetite NPs (a) are the characteristic peak of the intrinsic stretching vibrations modes for Fe–O bonds at the octahedral and tetrahedral cubic ferrite sites, respectively [30–32]. Meanwhile, the bands at 3396, 2347 and 1635 cm^{-1} are assigned to OH vibrations at the surface of the as-prepared magnetite NPs. The OH groups were inherited from the ethylene glycol molecules [33–35] and has higher vibrational intensities in Fe_3O_4 NPs over Fe_3O_4@C. The reduced vibrational intensities of these bands in Fe_3O_4@C indicate that, during glucose carbonisation, the carbon composited and effectively shielded the OH groups [36]. The peaks at 2848 and 2937 cm^{-1} are attributed to the antisymmetric and symmetric stretching vibration of C–H bonds introduced by ethylenediamine molecules at the solvothermal step for Fe_3O_4 NPs fabrication [37,38]. Weak to medium intensity peak at the 1385 cm^{-1} was ascribed to the antisymmetric C–N stretching vibrations coupled with the out-of-plane H–NH and N–H vibrational modes [33]. The peak at 870 cm^{-1} was assigned to the in-plane and out-of-plane vibrational modes for residual C–H bonds deformation [34]. Several peaks disappeared, shifted to new wavenumbers, or were retained in the resulting nanocomposites. Negligible shifts recorded for Fe–O bonds at the tetrahedral cubic ferrite sites and OH vibrations to 581 cm^{-1} and 3438–3449 cm^{-1}, respectively, indicate that the three nanocomposites retained the spectral characteristics of parent Fe_3O_4 NPs. The disappearance and shifting of some of the peaks in the spectra of the nanocomposites indicate the strong interaction between the parent Fe_3O_4 NPs core and the encapsulating carbon layer bounding its surface [35].
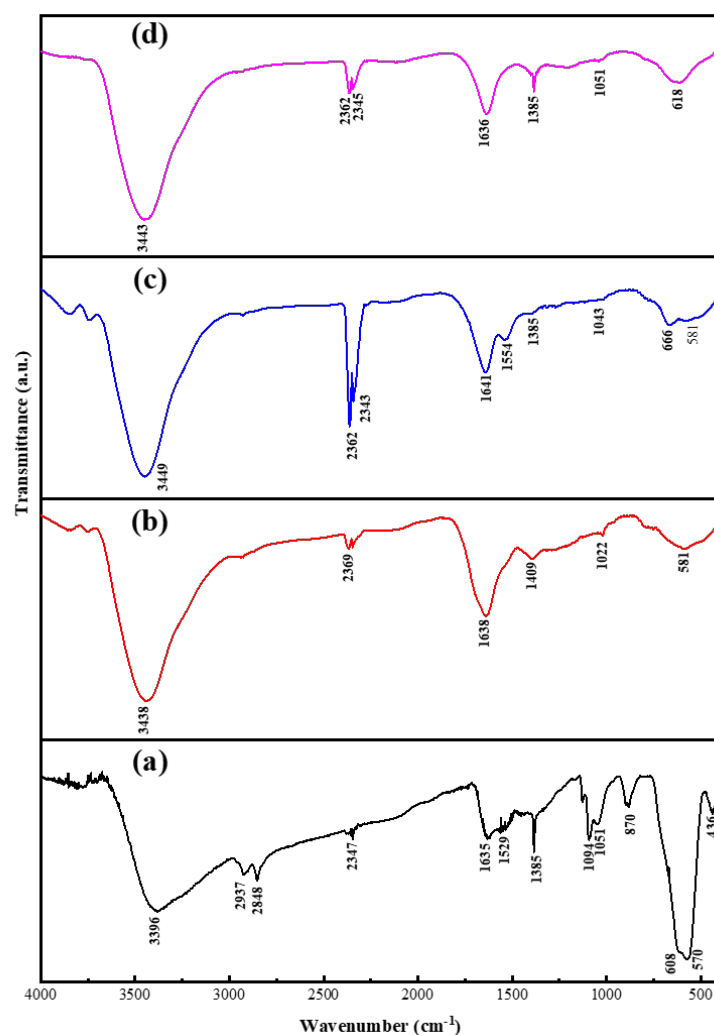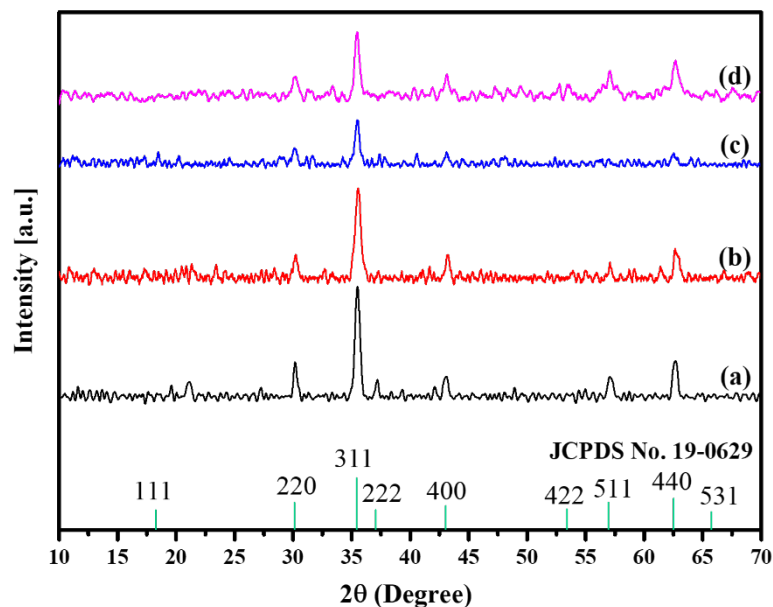
Figure 1. FTIR spectra for (**a**) Fe_3O_4 NPs; (**b**) $Fe_3O_4@C-T_{190}t_3$; (**c**) $Fe_3O_4@C-T_{190}t_4$; (**d**) $Fe_3O_4@C-T_{190}t_5$.

3.1.2. X-ray Diffraction Analysis

Crystal phases of the as-synthesised nanocomposites were investigated using an X-ray diffractometer, and the results are shown in Figure 2. The XRD patterns of $Fe_3O_4@C-T_{190}t_3$, $Fe_3O_4@C-T_{190}t_4$, and $Fe_3O_4@C-T_{190}t_5$ have diffraction peaks that matched the standard diffractogram of the magnetic Fe_3O_4 NPs (JCPDS No. 19-0629). The XRD peaks and crystal lattice constant (a_o) in all the XRD patterns with the magnetite standards information indexed in the ICDD database [35] were compared. The a_o values determined from the peaks with the highest intensity for $Fe_3O_4@C-T_{190}t_3$, $Fe_3O_4@C-T_{190}t_4$, $Fe_3O_4@C-T_{190}t_5$ were found to be 8.38, 8.37 and 8.38 Å, in agreement with the standard parameter for the magnetite (8.39 Å). The diffraction peaks at 2θ = 57.1°, 62.7°, 53.5°, 43.1°, 35.5°, 30.2° and 21.9° which can be assigned to the Miller indices planes (511), (440), (422), (400), (311), (220) and (111), respectively, corresponding to a cubic inverse spinel unit cell structure of Fe_3O_4 nanomaterials [36,37] were retained in all three $Fe_3O_4@C$ nanocomposites. The ability of the nanocomposites to retain the characteristic Miller indices planes identified in the parent Fe_3O_4 NPs after the synthesis is an indicator of their phase purity with respect to the Fe_3O_4 NPs. The XRD patterns of the $Fe_3O_4@C$ nanocomposites did not show sharp peaks at 2θ values of 26° and 54°, which are the characteristic peaks for crystalline carbons [38,39]. However, the broad background, typical of amorphous material, in the XRD diffractograms of the nanocomposites relative to that of the Fe_3O_4 NPs confirmed the amorphous nature of the encapsulating carbon layer [39–41] is also absent. Thus, the XRD peaks corresponding to the encapsulating carbons were not found in the XRD pattern because they were poorly

crystallised [42]. While the nature of the carbon layer may be ambiguous, the presence of the carbon layer in the nanocomposites is evidenced, especially from the thermal and EFTEM analysis.

Figure 2. X-ray diffraction patterns of (**a**) Fe_3O_4 NPs; (**b**) Fe_3O_4@C-$T_{190}t_3$; (**c**) Fe_3O_4@C-$T_{190}t_4$; (**d**) Fe_3O_4@C-$T_{190}t_5$.

The crystallite sizes (D_{hkl}) of the nanocomposite samples were determined using the well-known Scherrer equation (Equation (1)):

$$D_{hkl} = \frac{K\lambda}{\beta \cos\theta} \tag{1}$$

where θ is the half diffraction angle of 2θ, K is the constant (=0.94), λ is the wavelength (=0.15406 nm), β is the full width at half maximum (FWHM) value of XRD diffraction peaks. The average crystallite size (D_{XRD}) for each nanocomposite sample was calculated by dividing the total D_{hkl} values by the number of individual planes [26]. The average crystallite grain size (D_{XRD}) for each of the three nanocomposites (Fe_3O_4@C-$T_{190}t_3$, Fe_3O_4@C-$T_{190}t_4$, Fe_3O_4@C-$T_{190}t_5$) was computed to be 13 ± 8, 11 ± 6 and 16 ± 5 nm, respectively. The variation in the D_{XRD} values in the nanocomposites can be attributed to the extent of carbonisation of the carbons composited to the parent Fe_3O_4 NPs at different reaction times, which was also in line with the reported EFTEM outcomes. Previously, Xu et al. [43] reported similar values for the average Fe_3O_4 NPs crystallite size of their as-synthesised Fe_3O_4@C nanocomposites.

3.1.3. Thermogravimetric Analysis/Differential Thermogravimetry (TGA/DTG)

The thermograms of the as-synthesised Fe_3O_4@C nanocomposites and parent Fe_3O_4 NPs are illustrated in Figure 3. The recorded weight loss at 30–100 °C in Fe_3O_4@C-$T_{190}t_3$ (6.92%), Fe_3O_4@C-$T_{190}t_4$ (1.03%), and Fe_3O_4@C-$T_{190}t_5$ (5.37%) can be attributed to the evaporation of the water molecules physisorbed onto the surface of the samples. Degradation of the organic residue could probably be the factor responsible for the weight loss of 5.72–6.43% recorded within the temperature range of 100–300 °C for Fe_3O_4@C nanocomposites. The combustion of the encapsulating carbon was concurrently accomplished between 150 to 450 °C. The intensified degradation of organic residues and the carbonisation of the top layer of the Fe_3O_4@C nanocomposite surfaces could be asserted as the factor responsible for the weight loss recorded within the temperature range of 300–450 °C for Fe_3O_4@C-$T_{190}t_3$ (19.11%), Fe_3O_4@C-$T_{190}t_4$ (6.43%), and Fe_3O_4@C-$T_{190}t_5$ (19.55%). The

uptake of carbon deposits from the in situ carbonisations of glucose precursor molecules onto the parent Fe_3O_4 NPs was more favourable during the hydrothermal synthesis of Fe_3O_4@C-$T_{190}t_3$ and Fe_3O_4@C-$T_{190}t_5$ than for Fe_3O_4@C-$T_{190}t_4$. As a result, the carbon content of the encapsulating layers in Fe_3O_4@C-$T_{190}t_3$ and Fe_3O_4@C-$T_{190}t_5$ was higher than in Fe_3O_4@C-$T_{190}t_4$. At 300~450 °C, gasification of the encapsulated carbon layer of the nanocomposites occurs. The gasification rate of the encapsulating carbon layer per minute in Fe_3O_4@C-$T_{190}t_3$ and Fe_3O_4@C-$T_{190}t_5$ was higher than in Fe_3O_4@C-$T_{190}t_4$ (as shown in red by plots in Figure 3) due to the higher carbon content in the composites. Further weight loss at higher temperatures, i.e., 450–900 °C, for Fe_3O_4@C-$T_{190}t_3$ (27.63%), Fe_3O_4@C-$T_{190}t_4$ (23.34%), and Fe_3O_4@C-$T_{190}t_5$ (28.54%), could be assigned to intensified carbonisation of the nanocomposite topmost layer and probable total exposure of the magnetite core of the nanocomposites [44]. Based on the overall weight loss throughout the entire heating profile of 30–900 °C, Fe_3O_4@C-$T_{190}t_4$ (36.5%) is the most stable sample in agreement with the carbon content shown in EDX analysis below. The thermal stability of both Fe_3O_4@C-$T_{190}t_5$ and Fe_3O_4@C-$T_{190}t_3$ are relatively similar, with a weight loss of as much as 60.0%. Moreover, the magnetite NPs from which the composites were fabricated recorded a far lower weight loss of 17.4% within the heating profile of 30–700 °C. The corresponding Fe_3O_4 NPs weight contents in the nanocomposites were estimated to be ~63.5% for Fe_3O_4@C-$T_{190}t_4$ and ~40.3% for both Fe_3O_4@C-$T_{190}t_3$ and Fe_3O_4@C-$T_{190}t_5$ within the heating profile. Fe_3O_4 NPs weight contents indicate the encapsulating carbon content composited in each as-synthesised nanocomposite material. However, relatively higher estimations of Fe_3O_4 NPs content (95.5%), thus signifying lower carbon content, were reported by Xu et al. [43].
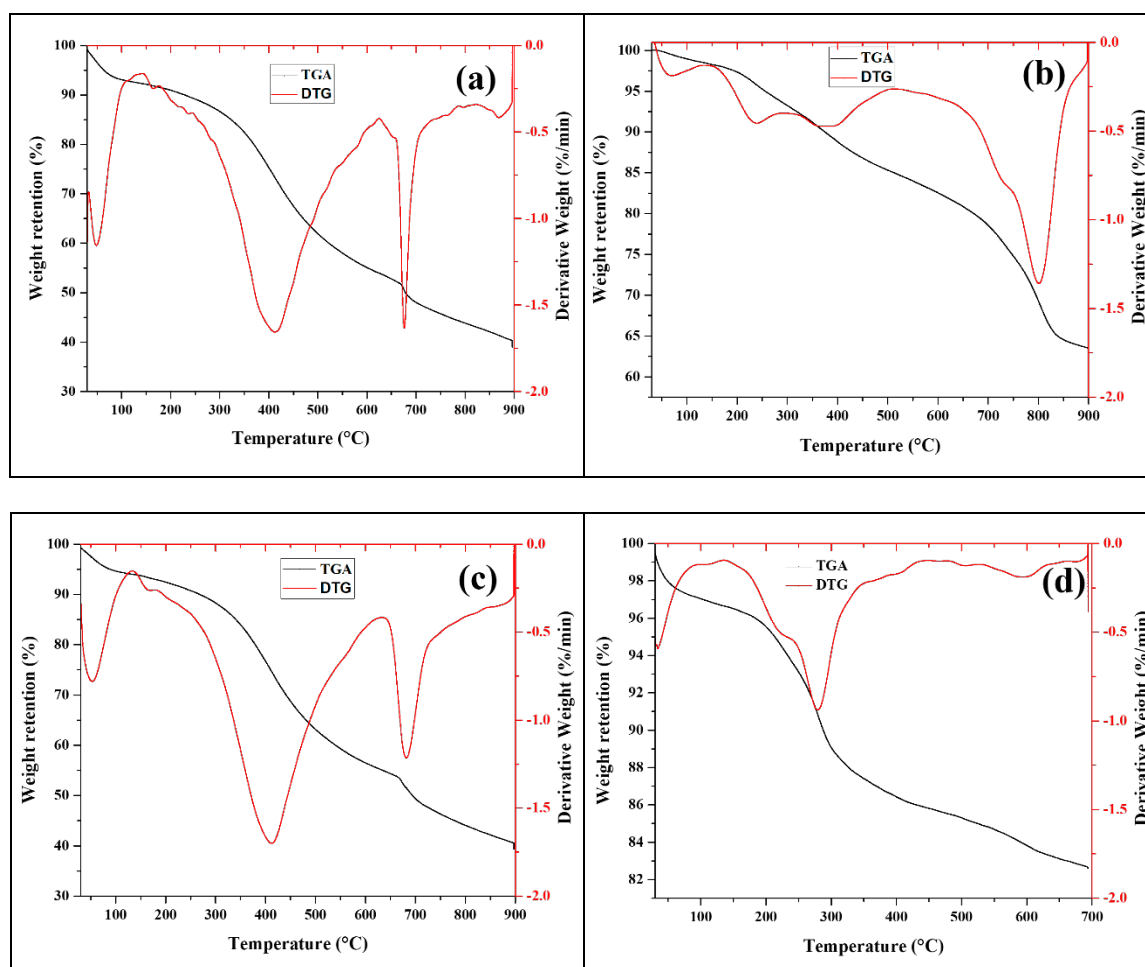

Figure 3. TGA/DTG curves for (**a**) Fe_3O_4@C-$T_{190}t_3$; (**b**) Fe_3O_4@C-$T_{190}t_4$; (**c**) Fe_3O_4@C-$T_{190}t_5$; (**d**) Fe_3O_4 NPs.

The TGA/DTG analysis was used to monitor the weight loss and thermal stability of the sample as the temperature increased. As the increased weight loss with temperature could not allow estimations of the parent Fe_3O_4 NPs, the EDX analysis was employed in the semiquantitative estimation of the Fe_3O_4 NPs weights present in each nanocomposites sample. The major compositional component of the composites, Fe_3O_4 NPs, is completely transformed to hematite within the temperature range of 600–675 °C. Thus, comparisons between the weight loss in the nanocomposites and the parent Fe_3O_4 NPs precursor were performed by truncating the temperature axes of the nanocomposites to 700 °C, making the difference in the studied temperature range among the nanomaterials inconsequential. Change in weight of the composites within the range 675–900 °C could be attributed to the continued gasification of the encapsulating carbon layer and further transformations of the parent Fe_3O_4 NPs core [45].

3.1.4. Scanning Electron Microscopy

Figure 4a–l compares the SEM micrographs of the as-synthesised Fe_3O_4@C nanocomposites and Fe_3O_4 NPs at low and high magnifications together with their EDX spectra. The SEM micrographs of Fe_3O_4@C-$T_{190}t_3$ (Figure 4a,b) and Fe_3O_4@C-$T_{190}t_5$ nanocomposites (Figure 4g,h) revealed the conspicuous formation of well-defined clusters of nanospheres during the hydrothermal process. In contrast, Fe_3O_4@C-$T_{190}t_4$ nanocomposite (Figure 4d,e) exhibit the formation of agglomerated clusters among the nanospheres. The nanocomposites show varying degrees of distributions in particle size, uniformity, and aggregation [46]. The nanocomposites possess larger distribution of particle size (11–91 nm) than the parent Fe_3O_4 NPs (21–39 nm), as indicated by supporting information from EFTEM, which is comparable to the observation reported by Liu et al. [44].

The EDX spectroscopic analyses (Figure 4c,f,i) carried out on the nanocomposites indicated the proportion by weight of carbon to increase in the order Fe_3O_4@C-$T_{190}t_4$ (14.1%) < Fe_3O_4@C-$T_{190}t_3$ (64.3%) < Fe_3O_4@C-$T_{190}t_5$ (72.4%). It could be observed that Fe_3O_4@C-$T_{190}t_4$ has the lowest carbon content and recorded the least weight loss. Although it was found to compose of a typical stoichiometry near the standard phase composition of Fe_3O_4 NPs (78.3% Fe, 21.7% O) by atomic weight, the as-synthesised magnetite NPs obtained at the solvothermal step has been observed to exhibit an experimental stoichiometric ratio O:Fe (0.28) a little less than the expected value (0.38) [47]. This observed deviation can be attributed to the fact that EDX is a semiquantitative analytical technique. Previously, based on EDX analysis, Liu et al. [44] reported that their as-synthesised Fe_3O_4@C nanocomposites contained 15.4% carbon, which is in agreement with Fe_3O_4@C-$T_{190}t_4$ (14.1%) but far lower than those observed for Fe_3O_4@C-$T_{190}t_3$ (64.3%) and Fe_3O_4@C-$T_{190}t_5$ (72.4%). This observation indicates that the deposition of the encapsulating carbon layer onto the parent Fe_3O_4 NPs was more favourable at 5 h, and the least favourable reaction time was at 4 h.
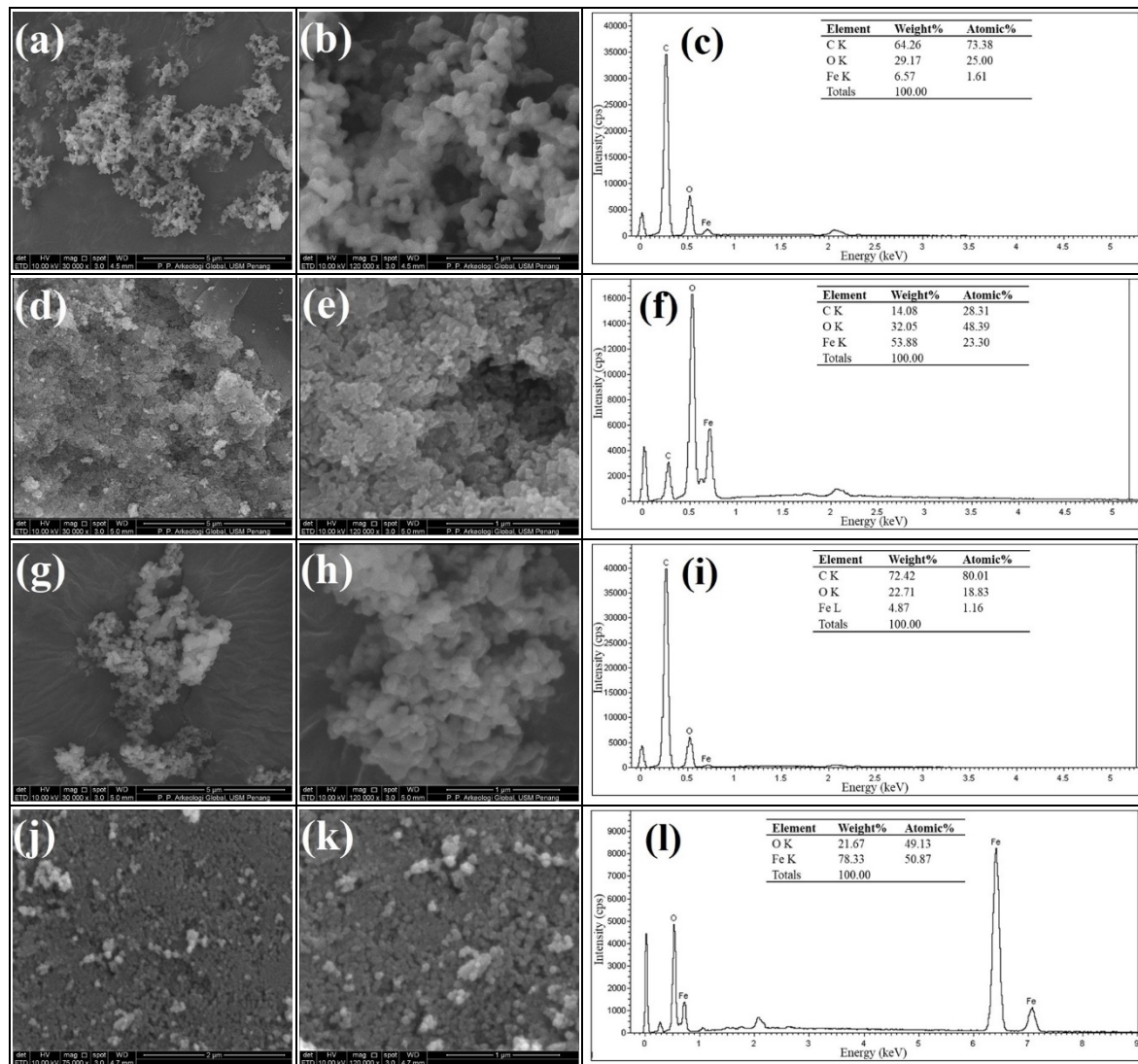
Figure 4. SEM images with different resolutions (30 k×, 120 k×) and EDX elemental composition of Fe_3O_4@C-$T_{190}t_3$ (**a–c**), Fe_3O_4@C-$T_{190}t_4$ (**d–f**), Fe_3O_4@C-$T_{190}t_5$ (**g–i**), and Fe_3O_4 NPs (**j–l**), respectively.

3.1.5. Transmission Electron Microscopy

Evaluations of particle size distribution and further morphological elucidation of the nanocomposites were carried out using the EFTEM characterisation technique. Figure 5 demonstrates differing compositions of spherical, rod-like, and cubic morphologies depending on the reaction time (t_r). The formation of nanocomposites with larger grain sizes has been conspicuously observed to be more favourable at t_r of 3 and 5 h, which in turn may be due to the amount of carbon in the nanocomposite. Figure 5a,d,g show the nanocomposites to appear as clusters of nanospheres while at higher magnifications (Figure 5b,e,h) they appear to be more cubic-like nanocomposites.
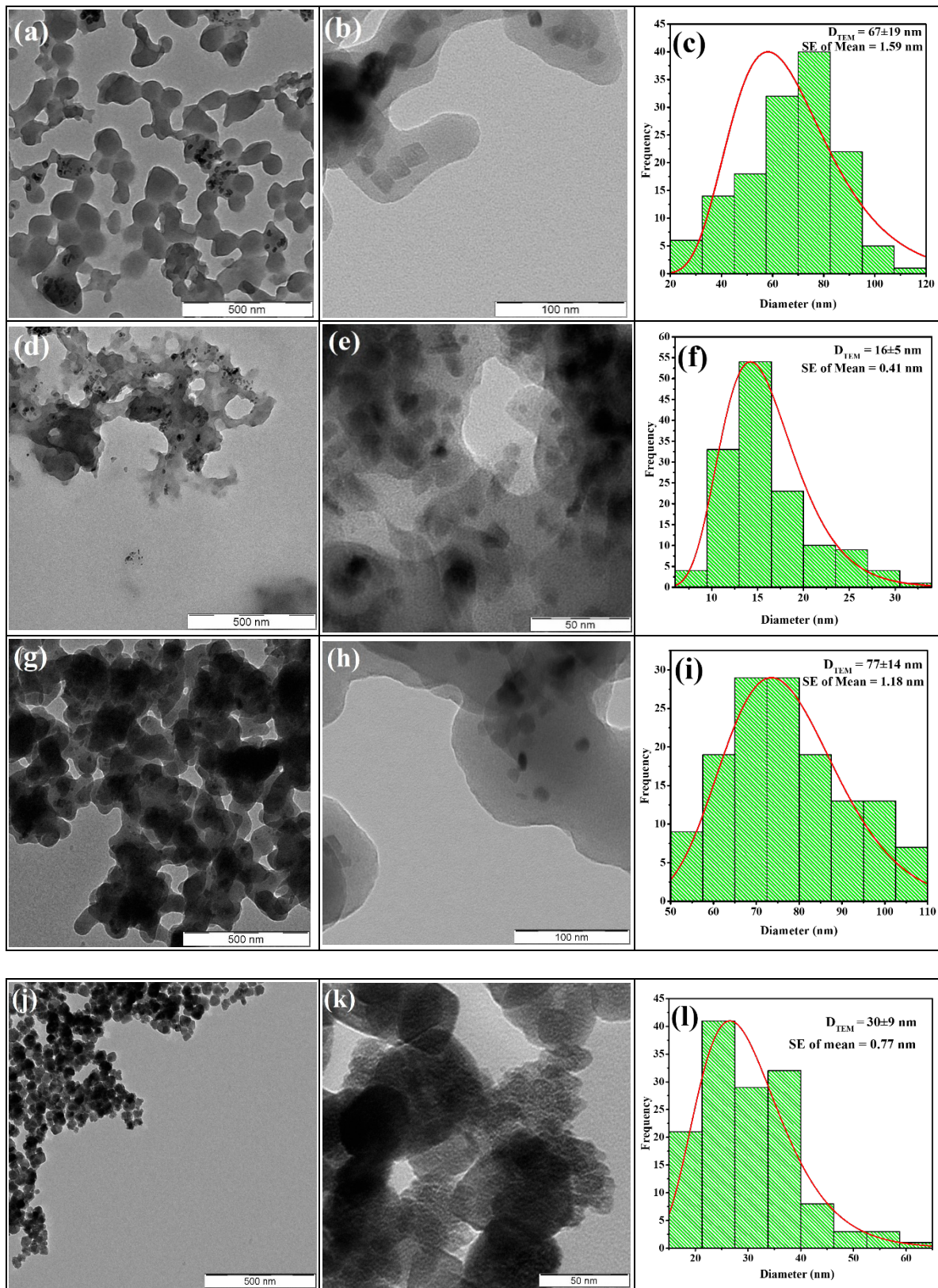
Figure 5. TEM images with different resolutions (12.5 k×, 100 k×) and particle size distributions of Fe_3O_4@C-$T_{190}t_3$ (**a–c**), Fe_3O_4@C-$T_{190}t_4$ (**d–f**), Fe_3O_4@C-$T_{190}t_5$ (**g–i**), and Fe_3O_4 NPs (**j–l**), respectively.

The nanocomposites' particle size distributions were evaluated by fitting a lognormal distribution function over histograms constructed from the edge length (or diameter) data

obtained via the measurements of 138 grains on the TEM micrograph of each sample. The Sturge's rule, expressed in Equation (2), was applied to evaluate the number of bins (k) for the histograms [48,49]:

$$k = 1 + \log_2 N \qquad (2)$$

where N is the sample size representing the number of measurements carried out on each EFTEM micrograph. The results show that the mean particle diameter (D_{TEM}) for the nanocomposites Fe_3O_4@C-$T_{190}t_3$, Fe_3O_4@C-$T_{190}t_4$ and Fe_3O_4@C-$T_{190}t_5$ were 67 ± 19, 16 ± 5, and 77 ± 14 nm, respectively, in contrast to the mean diameter of 30 ± 9 nm recorded for the parent Fe_3O_4 NPs (Figure 5l). Fe_3O_4@C-$T_{190}t_3$ and Fe_3O_4@C-$T_{190}t_5$ composites exhibited carbon shells of 37 and 47 nm in thickness, which were shells probably not observable in Fe_3O_4@C-$T_{190}t_4$ composite under the current microscopic settings as evidenced by its lowest carbon content from EDX analysis and lowest weight loss from the thermal analysis. Thus, the thickness of the carbon encapsulation at 3 h decreased at 4 h and then increased at 5 h, indicating that the thickness of the carbon layer from glucose resources can be controlled by increasing the reaction time [40]. The small standard error of the mean (0.41–1.59 nm) indicates that the values of the mean particle size (D_{TEM}) are accurate and reliable representations of measurements in each sample size [50]. Furthermore, nanocomposites with similar particle size distribution (30 ± 19 nm) were also reported in the literature [44].

3.1.6. Brunauer–Emmett–Teller (BET) Nitrogen Adsorption–Desorption Analysis

Figure 6 illustrates the comparison of the nitrogen adsorption–desorption isotherms for the as-synthesised Fe_3O_4@C nanocomposites and the magnetite NPs (Figure 6d). The BET isotherms of all the three nanocomposites exhibited an H3 hysteresis loop and were classified as Type II adsorption isotherms in line with International Union of Pure and Applied Chemistry (IUPAC). It is the characteristic of mesoporous materials whose mesopore volumes are not well defined because of the low-degree pore curvature and non-rigid structure of the aggregate nanocomposites [51–53]. The BET surface areas for the as-prepared magnetite composites are 12.39 m^2 g^{-1} (Fe_3O_4@C-$T_{190}t_3$), 22.41 m^2 g^{-1} (Fe_3O_4@C-$T_{190}t_4$), 7.61 m^2 g^{-1} (Fe_3O_4@C-$T_{190}t_5$), compared to 5.6 m^2 g^{-1} reported by Zeng and co-workers [20]. However, values as high as $\sim$342.7 m^2 g^{-1} have been reported by Zhuang and co-workers [23].

Various surface properties of the nanocomposites were further compared (Figure 7a–d). Different forms of the surface area including the BET surface area (S_{BET}), Langmuir surface area (S_{Lang}), t-plot surface area (S_{Ext}), Barrett-Joyner-Halenda (BJH) adsorption cumulative surface area of pores (S_{BJH}) and BJH desorption cumulative surface area of pores (S'_{BJH}) were compared in Figure 7a. Meanwhile, Figure 7b shows the comparison between the BET adsorption total pore volume (V_{BET}) with BJH adsorption total pore volume (V_{BJH}), BET desorption total pore volume (V'_{BET}), and BJH desorption total pore volume (V'_{BJH}) as pore volumes equivalents. In addition to that, the comparative distinction among BET adsorption average pore width (D_{BET}), BET desorption average pore width (D'_{BET}), BJH adsorption average pore width (D_{BJH}), and BJH desorption average pore width (D'_{BJH}) were presented in Figure 7c. Comparison between the mean crystallite size from XRD (D_{XRD}) and mean particle size from TEM (D_{TEM}) among the nanocomposites was presented in Figure 7d. The results show that Fe_3O_4@C-$T_{190}t_4$ has the highest surface area, total pore volumes and pore diameters and the smallest crystallite grain size and particle size among the three Fe_3O_4@C nanocomposites. However, the average surface area (114 m^2 g^{-1}), pore volume (0.21 cm^3 g^{-1}), and crystallite size (19 nm) of the parent Fe_3O_4 NPs were greater than those of the resulting composites. On the contrary, the average values of pore diameter and grain size of the parent Fe_3O_4 NPs (8.4, 30 nm) were both smaller than that of the Fe_3O_4@C-$T_{190}t_3$ (12.6, 67 nm) and Fe_3O_4@C-$T_{190}t_5$ (10.7, 77 nm) nanocomposites. Although the pore diameter of the Fe_3O_4 NPs (8.4 nm) was also less than that of the Fe_3O_4@C-$T_{190}t_4$ nanocomposite (17.4 nm), the grain size of the parent NPs (30 nm) was larger than in the nanocomposite (16 nm).
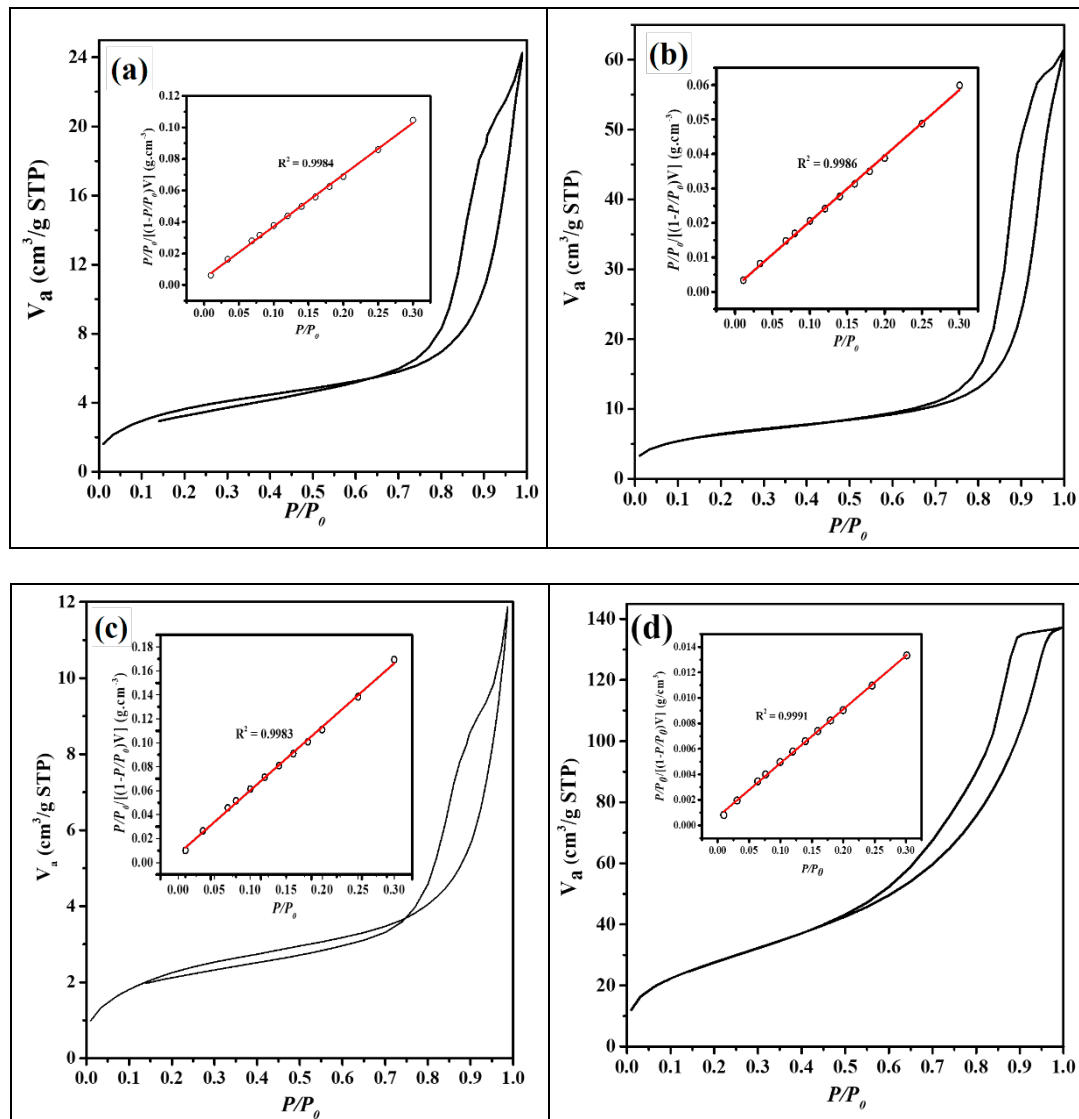
Figure 6. BET nitrogen adsorption–desorption hysteresis curves and linear isotherms (in the inset) of (**a**) Fe_3O_4@C-$T_{190}t_3$; (**b**) Fe_3O_4@C-$T_{190}t_4$; (**c**) Fe_3O_4@C-$T_{190}t_5$; (**d**) Fe_3O_4 NPs.
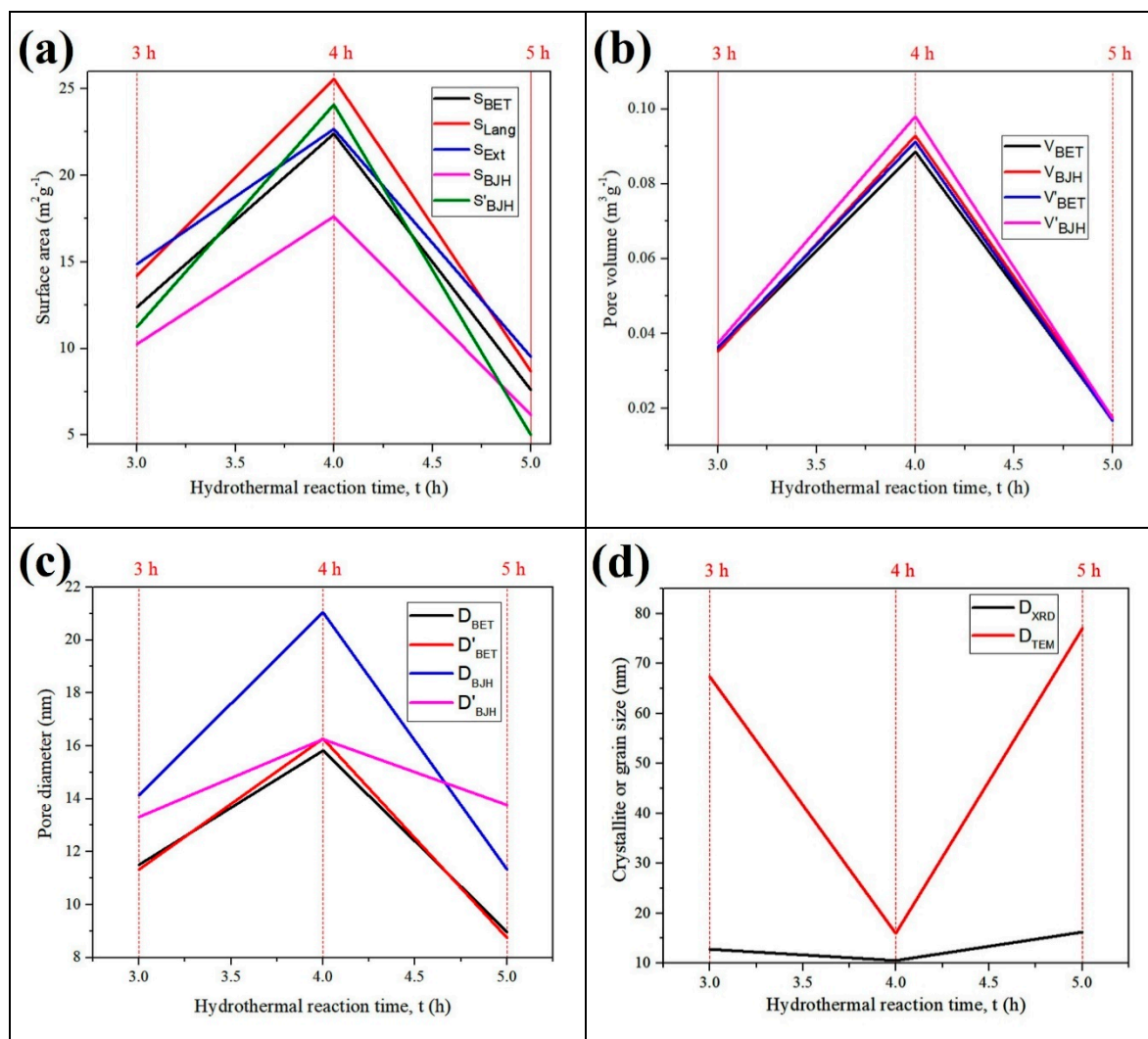
Figure 7. Effects of reaction time on the (**a**) surface area, (**b**) pore volume, (**c**) pore diameter and (**d**) crystallite or grain size of Fe_3O_4@C-$T_{190}t_3$, Fe_3O_4@C-$T_{190}t_4$ and Fe_3O_4@C-$T_{190}t_5$ nanocomposites obtained by hydrothermal synthesis.

3.2. Two-Step Fe_3O_4@C NCs Formation Mechanism

The mechanism of the process was accomplished in two steps. The solvothermal method was used to synthesise the mesoporous Fe_3O_4 NPs in the first step, whose mechanism was proposed by Li et al. [29]. According to the mechanism proposed, EG is employed both as a reducing agent and high boiling point solvent. Sodium acetate is incorporated in the reaction mixture to act as a structure-directing agent, while ethylenediamine (EDA) is added as a chelating solvent to the parent Fe_3O_4 NPs [54]. Specifically, glycolaldehyde is produced by oxidising EG in solvothermal heating. The glycolaldehyde obtained reduces Fe^{3+} to Fe^{2+} ion, resulting in glyoxal. The acetate anions (CH_3COO^-) combine with the free Fe^{3+} and Fe^{2+} cations in the mixture to produce the acetates, $Fe[CH_3COO]_3$ and $Fe[CH_3COO]_2$, as the temperature rises. At such high temperatures, hydrolysis and alcoholysis convert $Fe[CH_3COO]_3$ and $Fe[CH_3COO]_2$ into $Fe(OH)_3$ and $Fe(OH)_2$. Dehydration of the hydrolytic products eventually produces the parent Fe_3O_4 NPs. As a chelating agent, EDA facilitates the growth of the encapsulating carbon particles on the Fe_3O_4 NPs under hydrothermal reaction to fabricate Fe_3O_4@C NCs samples at various reaction times [54].

3.3. Statistical Analysis of the Surface Properties

3.3.1. Analysis of Variance (ANOVA)

Analysis of variance (ANOVA) was carried out to test the null hypothesis (H_0) that all means for the surface area, total pore volume and pore diameter for the three nanocomposites were equal at the 0.05 statistical level of significance (α). The corresponding alternative hypothesis (H_1) asserts that not all means of these surface properties of the nanocomposites were equal.

From the ANOVA results (Table 1), the hydrothermal t_r has been ascertained to affect the surface area significantly, total pore volumes and pore diameters for the three samples of the Fe_3O_4@C nanocomposites ($p < 0.05$). The summary of the model statistic (Table 2) was able to explain most of the variables to a great extent in total pore volumes ($R^2 = 99.60\%$) of the Fe_3O_4@C nanocomposites among the fabricated samples, followed by surface area ($R^2 = 90.13\%$). In comparison, the least variability was observed in the pore diameters ($R^2 = 69.83\%$).

Table 1. Analysis of variance for the surface properties of the nanocomposites.

Source	DF [1]	SS [2]	MS [3]	F Value	*p* Value
Surface area					
Reaction time, t_r (h)	2	585.25	292.626	54.79	0.000
Error	12	64.09	5.341		
Total	14	649.34			
Total pore volume					
Reaction time, t_r (h)	2	0.012364	0.006182	1117.55	0.000
Error	9	0.000050	0.000006		
Total	11	0.012414			
Pore diameter					
Reaction time, t_r (h)	2	94.19	47.093	10.42	0.005
Error	9	40.68	4.520		
Total	11	134.87			

[1] DF, degree of freedom; [2] SS, sum of squares; [3] MS, mean square.

Table 2. Model statistic summary for the surface properties of the nanocomposites throughout the hydrothermal reaction time profile.

Statistic	Surface Property		
	Surface Area	Total Pore Volume	Pore Diameter
S	2.31107	0.002352	2.12613
R^2	90.13%	99.60%	69.83%
R^2-adj	88.48%	99.51%	63.13%
R^2-pred	84.58%	99.29%	46.37%

3.3.2. Pairwise Comparisons for Surface Properties

Figure 8 presents the plots for the Tukey simultaneous tests and Fisher individual tests for pairwise differences between means surface properties (surface areas, pore volumes, pore diameters) of the nanocomposite samples obtained at various hydrothermal t_r values (Fe_3O_4@C-$T_{190}t_3$, Fe_3O_4@C-$T_{190}t_4$ and Fe_3O_4@C-$T_{190}t_5$) at 95% confidence intervals (CIs).

The confidence intervals (CIs) observed in the Tukey test plots (Figure 8a,c,e) for the difference in the pore diameter means ((0.59, 8.98), (−6.07, 2.33), (−10.85, −2.45)), total pore volume means ((0.05193, 0.06122), (−0.02365, −0.01435), −0.08022, −0.07093)), surface area means ((5.98, 13.77), (−9.08, −1.28), (−18.95, −11.16)) between the nanocomposites Fe_3O_4@C-$T_{190}t_4$ and Fe_3O_4@C-$T_{190}t_3$ (4–3), Fe_3O_4@C-$T_{190}t_5$ and Fe_3O_4@C-$T_{190}t_3$ (5–3), and Fe_3O_4@C-$T_{190}t_5$ and Fe_3O_4@C-$T_{190}t_4$ (5–4) do not include zero in their interval except for the difference in the pore diameter means (−6.07, 2.33) between Fe_3O_4@C-$T_{190}t_5$ and Fe_3O_4@C-$T_{190}t_3$ (5–3), respectively. Similarly, the observed confidence intervals (CIs)

in the Fisher test plots (Figure 8b,d,f) for the difference in the means of pore diameter ((1.38, 8.19), (−5.27, 1.53), (−10.05, −3.25)), the means for the total pore volume ((0.05281, 0.06034), (−0.02276, −0.01524), (−0.07934, −0.07181)), the means of the surface area ((6.69, 13.06), (−8.36, −2.00), (−18.24, −11.87)) between the nanocomposites $Fe_3O_4@C\text{-}T_{190}t_4$ and $Fe_3O_4@C\text{-}T_{190}t_3$ (4–3), $Fe_3O_4@C\text{-}T_{190}t_5$ and $Fe_3O_4@C\text{-}T_{190}t_3$ (5–3), and $Fe_3O_4@C\text{-}T_{190}t_5$ and $Fe_3O_4@C\text{-}T_{190}t_4$ (5–4) exclude zero in their interval with exception to the difference in the pore diameter means (−5.27, 1.53) between $Fe_3O_4@C\text{-}T_{190}t_5$ and $Fe_3O_4@C\text{-}T_{190}t_3$ (5–3), respectively. These outcomes indicate that for all the pairwise comparisons under Tukey and Fisher tests, the mean surface properties between the nanocomposite samples are significantly different statistically except for the mean total pore volumes between nanocomposites $Fe_3O_4@C\text{-}T_{190}t_5$ and $Fe_3O_4@C\text{-}T_{190}t_3$ (5–3).
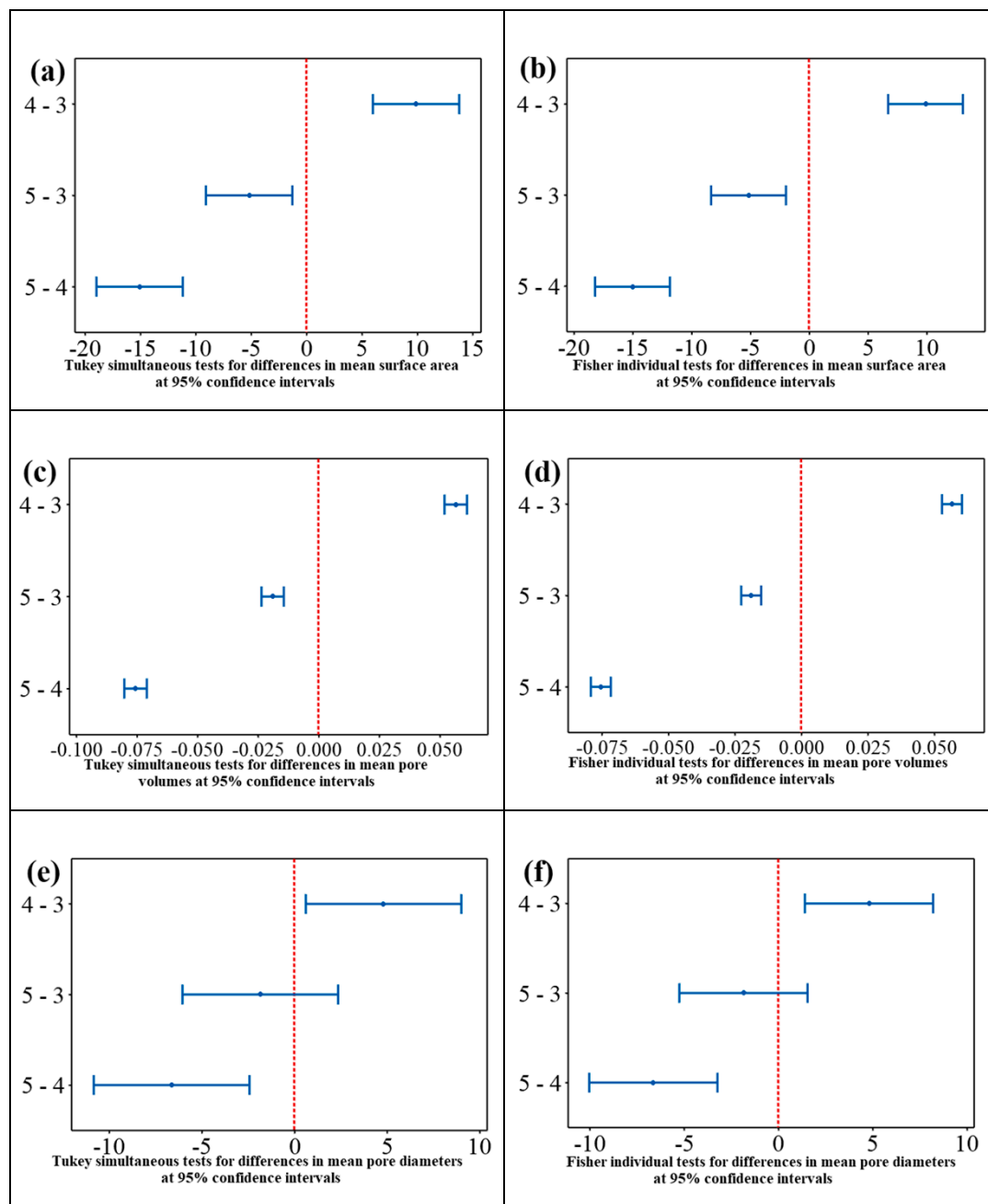
Figure 8. Tukey and Fisher tests of differences in means at 95% confidence intervals for (**a**,**b**) surface area, (**c**,**d**) pore volume, and (**e**,**f**) pore diameter of $Fe_3O_4@C$ nanocomposite samples obtained at various hydrothermal reaction times, respectively.

Table 3 tabulates the t values, individual confidence levels, adjusted p values, and simultaneous confidence levels from the Tukey and Fisher tests for all the pairwise differences in means for pore diameter, total pore volume and surface area of the nanocomposites. The t value test statistic measures the ratio between the difference in means of the surface properties and their standard errors in both the pairwise Tukey and Fisher tests between the nanocomposites. Observed absolute t values in both Tukey and Fisher tests for the difference in the pore diameter means (|3.18|, |1.24|, |4.42|), total pore volume means (|34.02|, |11.42|, |45.44|), surface area means (|6.76|, |3.54|, |10.30|) between the nanocomposites; Fe_3O_4@C-$T_{190}t_4$ and Fe_3O_4@C-$T_{190}t_3$ (4–3), Fe_3O_4@C-$T_{190}t_5$ and Fe_3O_4@C-$T_{190}t_3$ (5–3), and Fe_3O_4@C-$T_{190}t_5$ and Fe_3O_4@C-$T_{190}t_4$ (5–4) were found to be greater than their corresponding critical t values of 3.18, 3.18 and 2.78, respectively. This disparity indicates that the null hypothesis (H_0) that the mean properties are the same should be rejected, and the alternative hypothesis (H_1) that they are different should be accepted for all the nanocomposites in the pairwise comparative tests except for the difference in the pore diameter means between Fe_3O_4@C-$T_{190}t_5$ and Fe_3O_4@C-$T_{190}t_3$ (5–3). Since the absolute t values (|1.24|) for the difference in the pore diameter means between Fe_3O_4@C-$T_{190}t_5$ and Fe_3O_4@C-$T_{190}t_3$ (5–3) were less than the critical t values (3.18), the H_0 should be accepted.

Table 3. Significance statistic for Fisher individual tests and Tukey simultaneous tests on surface properties of the Fe_3O_4@C nanocomposite samples.

DOL [1]	DOM [2]	DSE [3]	T Value	Fisher Test		Tukey Test	
				ICL (%) [4]	p-adj [5]	SCL (%) [6]	p-adj [5]
Pore diameter							
4–3	4.79	1.50	3.18	97.91	0.011	88.66	0.027
5–3	−1.87	1.50	−1.24		0.246		0.460
5–4	−6.65	1.50	−4.42		0.002		0.004
Pore volume							
4–3	0.05658	0.00166	34.02	97.91	0.000	88.66	0.000
5–3	−0.01900	0.00166	−11.42		0.000		0.000
5–4	−0.07558	0.00166	−45.44		0.000		0.000
Surface area							
4–3	9.88	1.46	6.76	97.94	0.000	88.44	0.000
5–3	−5.18	1.46	−3.54		0.004		0.010
5–4	−15.06	1.46	−10.30		0.000		0.000

[1] DOL, difference of levels; [2] DOM, difference of means; [3] DSE, SE of difference; [4] ICL, individual confidence level; [5] p-adj, adjusted p value; [6] SCL, simultaneous confidence level.

The simultaneous confidence levels (SCLs) for pore diameter (88.66%), pore volume (88.66%) and surface area (88.44%) indicate that we can be 88.66%, 88.66% and 88.44% confident that all the corresponding confidence intervals contain the true difference for specific pairwise comparison of the nanocomposite properties. Meanwhile, the individual confidence levels (ICLs) for pore diameter (97.91%), pore volume (97.91%) and surface area (97.94) indicate that we can be 97.91%, 97.91%, and 97.94% confident that each of the corresponding confidence intervals contains the true difference.

The adjusted p values (p-adj) observed in both the Tukey and Fisher tests for the differences in means of the surface properties show that all the properties between the compared pairs of nanocomposites were statistically different (p-adj < 0.05), except for the difference in the mean total pore volumes between nanocomposites Fe_3O_4@C-$T_{190}t_5$ and Fe_3O_4@C-$T_{190}t_3$ (5–3), which is found to be statistically inconsequential (p-adj > 0.05).

The reaction time-dependent hydrothermal synthesis performed for surface properties optimisation produced mesoporous as-synthesised nanocomposites with high volume-specific surface area (VSSA) values. The order of the VSSA values for the nanocomposites are Fe_3O_4@C-$T_{190}t_5$ (4.48×10^{-8}) > Fe_3O_4@C-$T_{190}t_3$ (3.48×10^{-8}) > Fe_3O_4@C-$T_{190}t_4$ (2.53×10^{-8}). Large VSSA generally imparts nanomaterials unique surface characteristics,

including enhanced thermal, electrical, mechanical, and optical properties [55]. Moreover, the Fe_3O_4@C nanocomposites could be biocompatible with high response electrochemical activity, thermal stability, and enhanced thermal and electrical conductivity [56]. Such carbon-encapsulated magnetite nanomaterials have the potential for diverse applications in various fields. They can be used as drug carriers in targeted drug delivery therapeutic systems [57,58], anodes materials in the construction of electrochemical lithium-ion batteries [59], microwave absorbing material for the treatment of microwave radiation pollution [60–63], and coolants for heat transfer applications in various systems (e.g., automobile radiators, refrigerators, electronic devices, solar energy heaters, etc.) [56]. Fe_3O_4@C can also be applied as photothermal contrasting-agents in proton magnetic resonance imaging for cancer treatment [64], peroxidase enzymatic mimics for glucose sensing in human body fluids [65], and in the remediation of wastewater containing recalcitrant organic compounds either as adsorbent material [66,67] or as the catalyst [68,69]. The utilisation of Fe_3O_4@C nanocomposites as the catalysts for treating recalcitrant pollutants in palm oil mill effluent (POME) by advanced oxidation processes (AOPs) is a potential area for application of the nanocomposites.

4. Conclusions

Hydrothermal fabrications of carbon-encapsulated magnetite nanocomposites under a fixed temperature (190 °C) at reaction time (t_r) of 3 h (Fe_3O_4@C-$T_{190}t_3$), 4 h (Fe_3O_4@C-$T_{190}t_4$), and 5 h (Fe_3O_4@C-$T_{190}t_5$) have been accomplished. The influences of t_r on mean surface properties (surface area, total pore volumes and pore diameters) of the nanocomposites were evaluated using one-way analyses of variance (ANOVA), Tukey simultaneous tests and Fisher individual tests for differences in mean properties of nanocomposite pairs. The ANOVA test shows that the hydrothermal reaction time (t_r) significantly affected the surface area, total pore volumes and the particles size of the three Fe_3O_4@C nanocomposites samples ($p < 0.05$), and the model could explain almost 100%, 90% and 70% of the variability in the total pore volumes, surface area and pore diameters of the fabricated Fe_3O_4@C nanocomposites, respectively. These absolute t values from the pairwise comparison of the nanocomposites using Tukey and Fisher tests indicate the mean surface properties of nanocomposite pairs to be significantly different except for the mean total pore diameter of the pair Fe_3O_4@C-$T_{190}t_5$–Fe_3O_4@C-$T_{190}t_3$ (5-3). The adjusted p values (p-adj < 0.05) observed in the ANOVA for the pairwise difference in the mean properties further corroborated the outcome.

The levels of the mesoporosity, monodispersity, shape-controllability, and stability of the as-synthesised Fe_3O_4@C nanocomposite samples were established using FTIR, XRD, TGA/DTG, SEM/EDX, EFTEM and BET adsorption–desorption analyses. The as-synthesised nanocomposites largely retained the characteristic FTIR vibrations of the major absorption bands observed for Fe–O bond vibrations at the octahedral (436 cm^{-1}) and tetrahedral (570 cm^{-1}) cubic ferrite sites in the parent magnetite NPs with a shift in the latter band to 581 cm^{-1} and the shift in the OH vibrational assignments from 3396 to 3438–3449 cm^{-1}. The Fe_3O_4@C-$T_{190}t_5$ nanocomposite (16.3 ± 5.3 nm) recorded the largest mean for crystallite size, followed by Fe_3O_4@C-$T_{190}t_3$ (12.8 ± 7.8 nm) and finally Fe_3O_4@C-$T_{190}t_4$ (10.5 ± 6.4 nm). The TGA/DTG analyses revealed the Fe_3O_4@C-$T_{190}t_4$ nanocomposite to have the highest thermal stability with the lowest weight loss (36.5%). In comparison, Fe_3O_4@C-$T_{190}t_5$ and Fe_3O_4@C-$T_{190}t_3$ were less stable to heat with the higher weight loss (59.8–60.1%) in agreement with the carbon content of the Fe_3O_4@C composites from EDX analysis.

Author Contributions: Conceptualisation, S.S. and R.A.; methodology, S.S., R.A., W.-D.O. and A.I.; validation, S.S., R.A., W.-D.O. and A.I.; formal analysis, S.S. and R.A.; investigation, S.S.; resources, S.S., R.A., W.-D.O. and A.I.; data curation, S.S. and R.A.; writing—original draft preparation, S.S.; writing—review and editing, R.A.; visualisation, S.S. and R.A.; supervision, R.A.; project administration, R.A.; funding acquisition, S.S. and R.A. All authors have read and agreed to the published version of the manuscript.

Conflicts of Interest: The authors declare no conflict of interest. The funders had no role in the design of the study; in the collection, analyses, or interpretation of data; in the writing of the manuscript; or in the decision to publish the results.

References

1. Asab, G.; Zereffa, E.A.; Seghne, T.A. Synthesis of silica-coated Fe_3O_4 nanoparticles by microemulsion method: Characterization and evaluation of antimicrobial activity. *Int. J. Biomater.* **2020**, *2020*, 11. [CrossRef]

2. Abdel Maksoud, M.I.A.; Elgarahy, A.M.; Farrell, C.; Al-Muhtaseb, A.H.; Rooney, D.W.; Osman, A.I. Insight on water remediation application using magnetic nanomaterials and biosorbents. *Coord. Chem. Rev.* **2020**, *403*, 213096. [CrossRef]

3. Qi, M.; Zhang, K.; Li, S.; Wu, J.; Pham-Huy, C.; Diao, X.; Xiao, D.; He, H. Superparamagnetic Fe_3O_4 nanoparticles: Synthesis by a solvothermal process and functionalization for a magnetic targeted curcumin delivery system. *New J. Chem.* **2016**, *40*, 4480–4491. [CrossRef]

4. Yew, Y.P.; Shameli, K.; Miyake, M.; Ahmad Khairudin, N.B.B.; Mohamad, S.E.B.; Naiki, T.; Lee, K.X. Green biosynthesis of superparamagnetic magnetite Fe_3O_4 nanoparticles and biomedical applications in targeted anticancer drug delivery system: A review. *Arab. J. Chem.* **2020**, *13*, 2287–2308. [CrossRef]

5. Qin, L.; Ru, R.; Mao, J.; Meng, Q.; Fan, Z.; Li, X.; Zhang, G. Assembly of MOFs/polymer hydrogel derived Fe_3O_4-CuO@hollow carbon spheres for photochemical oxidation: Freezing replacement for structural adjustment. *Appl. Catal. B Environ.* **2020**, *269*, 118754. [CrossRef]

6. Xiong, L.L.; Huang, R.; Chai, H.H.; Yu, L.; Li, C.M. Facile synthesis of Fe_3O_4@Tannic Acid@Au nanocomposites as a catalyst for 4-nitrophenol and methylene blue removal. *ACS Omega* **2020**, *5*, 20903–20911. [CrossRef]

7. Vinodhkumar, G.; Wilson, J.; Inbanathan, S.S.R.; Potheher, I.V.; Ashokkumar, M.; Peter, A.C. Solvothermal synthesis of magnetically separable reduced graphene oxide/Fe_3O_4 hybrid nanocomposites with enhanced photocatalytic properties. *Phys. B Condens. Matter* **2020**, *580*, 411752. [CrossRef]

8. Ballarin, B.; Boanini, E.; Montalto, L.; Mengucci, P.; Nanni, D.; Parise, C.; Ragazzini, I.; Rinaldi, D.; Sangiorgi, N.; Sanson, A.; et al. PANI/Au/Fe_3O_4 nanocomposite materials for high performance energy storage. *Electrochim. Acta* **2019**, *322*, 134707. [CrossRef]

9. Pawar, S.P.; Melo, G.; Sundararaj, U. Dual functionality of hierarchical hybrid networks of multiwall carbon nanotubes anchored magnetite particles in soft polymer nanocomposites: Simultaneous enhancement in charge storage and microwave absorption. *Compos. Sci. Technol.* **2019**, *183*, 107802. [CrossRef]

10. Wang, L.; Lei, T.; Ren, Z.; Jiang, X.; Yang, X.; Bai, H.; Wang, S. Fe_3O_4@PDA@MnO_2 core-shell nanocomposites for sensitive electrochemical detection of trace Pb(II) in water. *J. Electroanal. Chem.* **2020**, *864*, 114065. [CrossRef]

11. Zhu, J.; Zhou, S.; Li, M.; Xue, A.; Zhao, Y.; Peng, W.; Xing, W. PVDF mixed matrix ultrafiltration membrane incorporated with deformed rebar-like Fe_3O_4–palygorskite nanocomposites to enhance strength and antifouling properties. *J. Memb. Sci.* **2020**, *612*, 118467. [CrossRef]

12. Ebrahimi-Tazangi, F.; Hekmatara, S.H.; Seyed-Yazdi, J. Synthesis and remarkable microwave absorption properties of amine-functionalized magnetite/graphene oxide nanocomposites. *J. Alloy. Compd.* **2019**, *809*, 151779. [CrossRef]

13. An, B.H.; Park, B.C.; Yassi, H.A.; Lee, J.S.; Park, J.R.; Kim, Y.K.; Ryu, J.E.; Choi, D.S. Fabrication of graphene-magnetite multi-granule nanocluster composites for microwave absorption application. *J. Compos. Mater.* **2019**, *53*, 4097–4103. [CrossRef]

14. Ma, C.; Liu, F.Y.; Wei, M.B.; Zhao, J.H.; Zhang, H.Z. Synthesis of novel core-shell magnetic Fe_3O_4@C nanoparticles with carboxyl function for use as an immobilisation agent to remediate lead-contaminated soils. *Polish J. Environ. Stud.* **2020**, *29*, 2273–2283. [CrossRef]

15. Suchanek, W.L.; Lencka, M.M.; Riman, R.E. Hydrothermal synthesis of ceramic materials. In *Aqueous Systems at Elevated Temperatures and Pressures*; Palmer, D.A., Prini, R.F., Harvey, A.H., Eds.; Elsevier Ltd.: Amsterdam, The Netherlands, 2004; pp. 716–744.

16. Moradiganjeh, J.; Aghajani, Z. Synthesis and characterization of novel magnetic Fe_3O_4/C through the co-precipitation method and investigation of its desulfurization application. *J. Mater. Sci. Mater. Electron.* **2016**, *27*, 5948–5953. [CrossRef]

17. Diodati, S.; Dolcet, P.; Casarin, M.; Gross, S. Pursuing the crystallization of mono- and polymetallic nanosized crystalline inorganic compounds by low-temperature wet-chemistry and colloidal routes. *Chem. Rev.* **2015**, *115*, 11449–11502. [CrossRef] [PubMed]

18. Darr, J.A.; Zhang, J.; Makwana, N.M.; Weng, X. Continuous hydrothermal synthesis of inorganic nanoparticles: Applications and future directions. *Chem. Rev.* **2017**, *117*, 11125–11238. [CrossRef]

19. Shi, W.; Song, S.; Zhang, H. Hydrothermal synthetic strategies of inorganic semiconducting nanostructures. *Chem. Soc. Rev.* **2013**, *42*, 5714–5743. [CrossRef]

20. Zeng, H.; Qiao, T.; Zhai, L.; Zhang, J.; Li, D. Fe$_3$O$_4$@C particles synthesized with iron-containing water treatment residuals and its potential for methylene blue removal. *J. Chem. Technol. Biotechnol.* **2019**, *94*, 3970–3980. [CrossRef]

21. Heidari, H.; Razmi, H. Multi-response optimization of magnetic solid phase extraction based on carbon coated Fe$_3$O$_4$ nanoparticles using desirability function approach for the determination of the organophosphorus pesticides in aquatic samples by HPLC-UV. *Talanta* **2012**, *99*, 13–21. [CrossRef]

22. Meng, X.; Yang, W.; Han, G.; Yu, Y.; Ma, S.; Liu, W.; Zhang, Z. Three-dimensional foam-like Fe$_3$O$_4$@C core-shell nanocomposites: Controllable synthesis and wideband electromagnetic wave absorption properties. *J. Magn. Magn. Mater.* **2020**, *502*, 1–10. [CrossRef]

23. Zhuang, Y.; Liu, J.; Yuan, S.; Ge, B.; Du, H.; Qu, C.; Chen, H.; Wu, C.; Li, W.; Zhang, Y. Degradation of octane using an efficient and stable core-shell Fe$_3$O$_4$@C during Fenton processes: Enhanced mass transfer, adsorption and catalysis. *Appl. Surf. Sci.* **2020**, *515*, 146083. [CrossRef]

24. Khoshsang, H.; Ghaffarinejad, A.; Kazemi, H.; Jabarian, S. Synthesis of mesoporous Fe$_3$O$_4$ and Fe$_3$O$_4$/C nanocomposite for removal of hazardous dye from aqueous media. *J. Water Environ. Nanotechnol.* **2018**, *3*, 191–206. [CrossRef]

25. Han, S.; Hu, L.; Liang, Z.; Wageh, S.; Al-Ghamdi, A.A.; Chen, Y.; Fang, X. One-step hydrothermal synthesis of 2D hexagonal nanoplates of α-Fe$_2$O$_3$/graphene composites with enhanced photocatalytic activity. *Adv. Funct. Mater.* **2014**, *24*, 5719–5727. [CrossRef]

26. Cao, B.; Adutwum, L.A.; Oliynyk, A.O.; Luber, E.J.; Olsen, B.C.; Mar, A.; Buriak, J.M. How to optimize materials and devices via design of experiments and machine learning: Demonstration using organic photovoltaics. *ACS Nano* **2018**, *12*, 7434–7444. [CrossRef]

27. Subramanian, V.; Zhu, H.; Vajtai, R.; Ajayan, P.M.; Wei, B. Hydrothermal synthesis and pseudocapacitance properties of MnO$_2$ nanostructures. *J. Phys. Chem. B* **2005**, *109*, 20207–20214. [CrossRef] [PubMed]

28. He, Q.; Liu, J.; Liang, J.; Liu, X.; Ding, Z.; Tuo, D.; Li, W. Sodium acetate orientated hollow/mesoporous magnetite nanoparticles: Facile synthesis, characterization and formation mechanism. *Appl. Sci.* **2018**, *8*, 292. [CrossRef]

29. Li, S.K.; Huang, F.Z.; Wang, Y.; Shen, Y.H.; Qiu, L.G.; Xie, A.J.; Xu, S.J. Magnetic Fe$_3$O$_4$@C@Cu$_2$O composites with bean-like core/shell nanostructures: Synthesis, properties and application in recyclable photocatalytic degradation of dye pollutants. *J. Mater. Chem.* **2011**, *21*, 7459–7466. [CrossRef]

30. Karaoğlu, E.; Baykal, A.; Erdemi, H.; Alpsoy, L.; Sozeri, H. Synthesis and characterization of dl-thioctic acid (DLTA)-Fe$_3$O$_4$ nanocomposite. *J. Alloys Compd.* **2011**, *509*, 9218–9225. [CrossRef]

31. Unal, B.; Durmus, Z.; Kavas, H.; Baykal, A.; Toprak, M.S. Synthesis, conductivity and dielectric characterization of salicylic acid-Fe$_3$O$_4$ nanocomposite. *Mater. Chem. Phys.* **2010**, *123*, 184–190. [CrossRef]

32. Unal, B.; Toprak, M.S.; Durmus, Z.; Sözeri, H.; Baykal, A. Synthesis, structural and conductivity characterization of alginic acid-Fe$_3$O$_4$ nanocomposite. *J. Nanoparticle Res.* **2010**, *12*, 3039–3048. [CrossRef]

33. Samadaei, F.; Salami-Kalajahi, M.; Roghani-Mamaqani, H.; Banaei, M. A structural study on ethylenediamine- and poly(amidoamine)-functionalized graphene oxide: Simultaneous reduction, functionalization, and formation of 3D structure. *RSC Adv.* **2015**, *5*, 71835–71843. [CrossRef]

34. Shen, L.; Li, B.; Qiao, Y.; Song, J. Monodisperse Fe$_3$O$_4$/SiO$_2$ and Fe$_3$O$_4$/SiO$_2$/PPy core-shell composite nanospheres for IBU loading and release. *Materials* **2019**, *12*, 828. [CrossRef] [PubMed]

35. Ardelean, I.L.; Stoencea, L.B.N.; Ficai, D.; Ficai, A.; Trusca, R.; Vasile, B.S.; Nechifor, G.; Andronescu, E. Development of Stabilized Magnetite Nanoparticles for Medical Applications. *J. Nanomater.* **2017**, *2017*. [CrossRef]

36. Zhang, D.; Shang, L.; Shen, J.; Shi, Z.; Wu, L.; Tung, C.; Zhang, T. A mild one-step solvothermal route to truncated octahedral magnetite crystals. *Particuology* **2014**, *15*, 51–55. [CrossRef]

37. Xu, J.; Yang, H.; Fu, W.; Du, K.; Sui, Y.; Chen, J.; Zeng, Y.; Li, M.; Zou, G. Preparation and magnetic properties of magnetite nanoparticles by sol–gel method. *J. Magn. Magn. Mater.* **2007**, *309*, 307–311. [CrossRef]

38. Saraswati, T.E.; Maharani, D.; Widiyandari, H. Copper oxide-based carbonaceous nanocomposites: Electrochemical synthesis and characterization. *AIP Conf. Proc.* **2020**, *2243*. [CrossRef]

39. Itoh, M.; Liu, J.R.; Horikawa, T.; Machida, K.I. Electromagnetic wave absorption properties of nanocomposite powders derived from intermetallic compounds and amorphous carbon. *J. Alloys Compd.* **2006**, *408–412*, 1400–1403. [CrossRef]

40. Shi, D.; Yang, H.; Ji, S.; Jiang, S.; Liu, X.; Zhang, D. Preparation and characterization of core-shell structure Fe$_3$O$_4$@C magnetic nanoparticles. *Procedia Eng.* **2015**, *102*, 1555–1562. [CrossRef]

41. Yuan, S.M.; Li, J.X.; Yang, L.T.; Su, L.W.; Liu, L.; Zhou, Z. Preparation and lithium storage performances of mesoporous Fe$_3$O$_4$@C microcapsules. *ACS Appl. Mater. Interfaces* **2011**, *3*, 705–709. [CrossRef] [PubMed]

42. Zhang, W.M.; Wu, X.L.; Hu, J.S.; Guo, Y.G.; Wan, L.J. Carbon coated Fe$_3$O$_4$ nanospindles as a superior anode material for lithium-ion batteries. *Adv. Funct. Mater.* **2008**, *18*, 3941–3946. [CrossRef]

43. Xu, J.L.; Zhang, X.; Miao, Y.X.; Wen, M.X.; Yan, W.J.; Lu, P.; Wang, Z.R.; Sun, Q. In-situ plantation of Fe$_3$O$_4$@C nanoparticles on reduced graphene oxide nanosheet as high-performance anode for lithium/sodium-ion batteries. *Appl. Surf. Sci.* **2021**, *546*, 149163. [CrossRef]

44. Liu, J.; Dong, S.; He, Q.; Yang, S.; Xie, M.; Deng, P.; Xia, Y.; Li, G. Facile preparation of Fe$_3$O$_4$/C nanocomposite and its application for cost-effective and sensitive detection of tryptophan. *Biomolecules* **2019**, *9*, 245. [CrossRef] [PubMed]

45. Ong, B.H.; Devaraj, N.K.; Matsumoto, M.; Abdullah, M.H. Thermal stability of magnetite (Fe_3O_4) nanoparticles. *Mater. Res. Soc. Symp. Proc.* **2009**, *1118*, 1–7. [CrossRef]

46. Fatima, H.; Lee, D.W.; Yun, H.J.; Kim, K.S. Shape-controlled synthesis of magnetic Fe_3O_4 nanoparticles with different iron precursors and capping agents. *RSC Adv.* **2018**, *8*, 22917–22923. [CrossRef]

47. Arenas-Alatorre, J.; Tehuacanero, C.S.; Lukas, O.; Rodríguez-Gómez, A.; Hernández Reyes, R.; Tapia-del León, C.; Lara V., J. Synthesis and characterization of iron oxide nanoparticles grown via a non-conventional chemical method using an external magnetic field. *Mater. Lett.* **2019**, *242*, 13–16. [CrossRef]

48. Aragón, F.H.; Coaquira, J.A.H.; Villegas-Lelovsky, L.; Da Silva, S.W.; Cesar, D.F.; Nagamine, L.C.C.M.; Cohen, R.; Menéndez-Proupin, E.; Morais, P.C. Evolution of the doping regimes in the Al-doped SnO_2 nanoparticles prepared by a polymer precursor method. *J. Phys. Condens. Matter* **2015**, *27*. [CrossRef]

49. Maboudi, S.A.; Shojaosadati, S.A.; Arpanaei, A. Synthesis and characterization of multilayered nanobiohybrid magnetic particles for biomedical applications. *Mater. Des.* **2017**, *115*, 317–324. [CrossRef]

50. Biau, D.J. In brief: Standard deviation and standard error. *Clin. Orthop. Relat. Res.* **2011**, *469*, 2661–2664. [CrossRef] [PubMed]

51. Mohan, D.; Sarswat, A.; Singh, V.K.; Alexandre-Franco, M.; Pittman, C.U. Development of magnetic activated carbon from almond shells for trinitrophenol removal from water. *Chem. Eng. J.* **2011**, *172*, 1111–1125. [CrossRef]

52. Wang, W.; Liu, P.; Zhang, M.; Hu, J.; Xing, F. The pore structure of phosphoaluminate cement. *Open J. Compos. Mater.* **2012**, *02*, 104–112. [CrossRef]

53. Kumari, M.; Pittman, C.U.; Mohan, D. Heavy metals [chromium (VI) and lead (II)] removal from water using mesoporous magnetite (Fe_3O_4) nanospheres. *J. Colloid Interface Sci.* **2015**, *442*, 120–132. [CrossRef] [PubMed]

54. Zhu, J.; Nan, Z. Zn-Doped Fe_3O_4 nanosheet formation induced by EDA with high magnetization and an investigation of the formation mechanism. *Am. Chem. Soc.* **2017**, *121*. [CrossRef]

55. Wohlleben, W.; Mielke, J.; Bianchin, A.; Ghanem, A.; Freiberger, H.; Rauscher, H.; Gemeinert, M.; Hodoroaba, V.D. Reliable nanomaterial classification of powders using the volume-specific surface area method. *J. Nanoparticle Res.* **2017**, *19*. [CrossRef]

56. Imran, M.; Zouli, N.; Ahamad, T.; Alshehri, S.M.; Chandan, M.R.; Hussain, S.; Aziz, A.; Dar, M.A.; Khan, A. Carbon-coated Fe_3O_4 core-shell superparamagnetic nanoparticle-based ferrofluid for heat transfer applications. *Nanoscale Adv.* **2021**, *3*, 1962–1975. [CrossRef]

57. Sousa, A.C.C.; Romo, A.I.B.; Almeida, R.R.; Silva, A.C.C.; Fechine, L.M.U.; Brito, D.H.A.; Freire, R.M.; Pinheiro, D.P.; Silva, L.M.R.; Pessoa, O.D.L.; et al. Starch-based magnetic nanocomposite for targeted delivery of hydrophilic bioactives as anticancer strategy. *Carbohydr. Polym.* **2021**, *264*. [CrossRef]

58. Asmatulu, R.; Fakhari, A.; Wamocha, H.L.; Chu, H.Y.; Chen, Y.Y.; Eltabey, M.M.; Hamdeh, H.H.; Ho, J.C. Drug-carrying magnetic nanocomposite particles for potential drug delivery systems. *J. Nanotechnol.* **2009**, *2009*, 1–6. [CrossRef]

59. Zhang, R.; Bao, S.; Tan, Q.; Li, B.; Wang, C.; Shan, L.; Wang, C.; Xu, B. Facile synthesis of a rod-like porous carbon framework confined magnetite nanoparticle composite for superior lithium-ion storage. *J. Colloid Interface Sci.* **2021**, *600*, 602–612. [CrossRef] [PubMed]

60. Xu, J.; Liu, Z.; Li, Q.; Wang, Y.; Shah, T.; Ahmad, M.; Zhang, Q.; Zhang, B. Wrinkled Fe_3O_4@C magnetic composite microspheres: Regulation of magnetic content and their microwave absorbing performance. *J. Colloid Interface Sci.* **2021**, *601*, 397–410. [CrossRef]

61. Zhang, M.; Ling, H.; Ding, S.; Xie, Y.; Cheng, T.; Zhao, L.; Wang, T.; Bian, H.; Lin, H.; Li, Z.; et al. Synthesis of CF@PANI hybrid nanocomposites decorated with Fe_3O_4 nanoparticles towards excellent lightweight microwave absorber. *Carbon* **2021**, *174*, 248–259. [CrossRef]

62. Li, Z.; Lin, H.; Ding, S.; Ling, H.; Wang, T.; Miao, Z.; Zhang, M.; Meng, A.; Li, Q. Synthesis and enhanced electromagnetic wave absorption performances of Fe_3O_4@C decorated walnut shell-derived porous carbon. *Carbon* **2020**, *167*, 148–159. [CrossRef]

63. Zhou, X.; Zhang, C.; Zhang, M.; Feng, A.; Qu, S.; Zhang, Y.; Liu, X.; Jia, Z.; Wu, G. Synthesis of Fe_3O_4/carbon foams composites with broadened bandwidth and excellent electromagnetic wave absorption performance. *Compos. Part A Appl. Sci. Manuf.* **2019**, *127*, 105627. [CrossRef]

64. Wu, F.; Sun, B.; Chu, X.; Zhang, Q.; She, Z.; Song, S.; Zhou, N.-L.; Zhang, J.; Yi, X.; Wu, D.; et al. Hyaluronic acid-modified porous carbon-coated Fe_3O_4 nanoparticles for magnetic resonance imaging-guided photothermal/chemotherapy of tumors. *Langmuir* **2019**, *35*, 13135–13144. [CrossRef]

65. Li, Q.; Tang, G.; Xiong, X.; Cao, Y.; Chen, L.; Xu, F.; Tan, H. Carbon coated magnetite nanoparticles with improved water-dispersion and peroxidase-like activity for colorimetric sensing of glucose. *Sensors Actuators, B Chem.* **2015**, *215*, 86–92. [CrossRef]

66. Bao, X.; Qiang, Z.; Chang, J.H.; Ben, W.; Qu, J. Synthesis of carbon-coated magnetic nanocomposite (Fe_3O_4@C) and its application for sulfonamide antibiotics removal from water. *J. Environ. Sci.* **2014**, *26*, 962–969. [CrossRef]

67. Wang, Y.; Ding, G.; Lin, K.; Liu, Y.; Deng, X.; Li, Q. Facile one-pot synthesis of ultrathin carbon layer encapsulated magnetite nanoparticle and graphene oxide nanocomposite for efficient removal of metal ions. *Sep. Purif. Technol.* **2021**, *266*. [CrossRef]

68. Chishti, A.N.; Guo, F.; Aftab, A.; Ma, Z.; Liu, Y.; Chen, M.; Gautam, J.; Chen, C.; Ni, L.; Diao, G. Synthesis of silver doped Fe_3O_4/C nanoparticles and its catalytic activities for the degradation and reduction of methylene blue and 4-nitrophenol. *Appl. Surf. Sci.* **2021**, *546*, 149070. [CrossRef]

69. Kakavandi, B.; Takdastan, A.; Jaafarzadeh, N.; Azizi, M.; Mirzaei, A.; Azari, A. Application of Fe_3O_4@C catalyzing heterogeneous UV-Fenton system for tetracycline removal with a focus on optimization optimisation by a response surface method. *J. Photochem. Photobiol. A Chem.* **2016**, *314*, 178–188. [CrossRef]